# Spreading and convective dissolution of carbon dioxide in vertically confined, horizontal aquifers

Christopher W. MacMinn,[1,2] Jerome A. Neufeld,[3,4] Marc A. Hesse,[5] and Herbert E. Huppert[4,6]

Received 17 April 2012; revised 21 September 2012; accepted 6 October 2012; published 13 November 2012.

[1] Injection of carbon dioxide ($CO_2$) into saline aquifers is a promising tool for reducing anthropogenic $CO_2$ emissions. At reservoir conditions, the injected $CO_2$ is buoyant relative to the ambient groundwater. The buoyant plume of $CO_2$ rises toward the top of the aquifer and spreads laterally as a gravity current, presenting the risk of leakage into shallower formations via a fracture or fault. In contrast, the mixture that forms as the $CO_2$ dissolves into the ambient water is denser than the water and sinks, driving a convective process that enhances $CO_2$ dissolution and promotes stable long-term storage. Motivated by this problem, we study convective dissolution from a buoyant gravity current as it spreads along the top of a vertically confined, horizontal aquifer. We conduct laboratory experiments with analog fluids (water and a mixture of methanol and ethylene glycol) and compare the experimental results with simple theoretical models. Since the aquifer has a finite thickness, dissolved buoyant fluid accumulates along the bottom of the aquifer, and this mixture spreads laterally as a dense gravity current. When dissolved buoyant fluid accumulates slowly, our experiments show that the spreading of the buoyant current is characterized by a parabola-like advance and retreat of its leading edge. When dissolved buoyant fluid accumulates quickly, the retreat of the leading edge slows as further dissolution is controlled by the slumping of the dense gravity current. We show that simple theoretical models predict this behavior in both limits, where the accumulation of dissolved buoyant fluid is either negligible or dominant. Finally, we apply one of these models to a plume of $CO_2$ in a saline aquifer. We show that the accumulation of dissolved $CO_2$ in the water can increase the maximum extent of the $CO_2$ plume by several fold and the lifetime of the $CO_2$ plume by several orders of magnitude.

**Citation:** MacMinn, C. W., J. A. Neufeld, M. A. Hesse, and H. E. Huppert (2012), Spreading and convective dissolution of carbon dioxide in vertically confined, horizontal aquifers, *Water Resour. Res.*, *48*, W11516, doi:10.1029/2012WR012286.

## 1. Introduction

[2] Injection of carbon dioxide ($CO_2$) into saline aquifers is a promising tool for reducing atmospheric $CO_2$ emissions [*Lackner*, 2003; *Intergovernmental Panel on Climate Change*, 2005; *Bickle*, 2009; *Orr*, 2009; *Szulczewski et al.*, 2012]. Permanently trapping the injected $CO_2$ is essential to minimize the risk of leakage into shallower formations. Leakage is a primary concern because the plume of injected $CO_2$ is buoyant relative to the ambient groundwater at representative aquifer conditions, and will rise toward the top of the aquifer after injection and spread laterally as a buoyant gravity current.

[3] One mechanism that acts to trap the buoyant $CO_2$ is the dissolution of free-phase $CO_2$ into the groundwater. Dissolved $CO_2$ is securely stored within the subsurface because it is no longer buoyant: the density of water increases with dissolved $CO_2$ concentration, so groundwater containing dissolved $CO_2$ will sink toward the bottom of the aquifer. As this mixture sinks in dense, $CO_2$-rich fingers, the resulting convective flow sweeps fresh groundwater upward. This convective dissolution process greatly enhances the rate at which the $CO_2$ dissolves into the groundwater [*Weir et al.*, 1996; *Lindeberg and Wessel-Berg*, 1997; *Ennis-King et al.*, 2005; *Riaz et al.*, 2006; *Hidalgo and Carrera*, 2009; *Pau et al.*, 2010; *Kneafsey and Pruess*, 2010; *Neufeld et al.*, 2010].

[4] Estimates of the impact of convective dissolution on the lifetime and distribution of a plume of $CO_2$ in the subsurface are essential for risk assessment. Recent numerical and experimental work has led to a greatly improved

[1]Department of Mechanical Engineering, Massachusetts Institute of Technology, Cambridge, Massachusetts, USA.
[2]Department of Geology and Geophysics and Department of Mechanical Engineering and Materials Science, Yale University, New Haven, Connecticut, USA.
[3]BP Institute and Department of Earth Sciences, University of Cambridge, Cambridge, UK.
[4]Institute of Theoretical Geophysics, Department of Applied Mathematics and Theoretical Physics, University of Cambridge, Cambridge, UK.
[5]Department of Geological Sciences and Institute for Computational Engineering and Sciences, University of Texas at Austin, Austin, Texas, USA.
[6]School of Mathematics, University of New South Wales, Sydney, New South Wales, Australia.

Corresponding author: C. W. MacMinn, Department of Geology and Geophysics, Yale University, PO Box 208109, New Haven, CT 06520-8109, USA. (christopher.macminn@yale.edu)


0043-1397/12/2012WR012286

understanding of both the onset [*Ennis-King et al.*, 2005; *Riaz et al.*, 2006; *Hidalgo and Carrera*, 2009; *Slim and Ramakrishnan*, 2010; *Backhaus et al.*, 2011] and the subsequent rate of the convective dissolution of a stationary layer of $CO_2$ overlying a reservoir of water [*Kneafsey and Pruess*, 2010; *Pau et al.*, 2010; *Neufeld et al.*, 2010; *Backhaus et al.*, 2011]. These results have been used to incorporate upscaled models for convective dissolution into models for the spreading and migration of buoyant plumes of $CO_2$ after injection [*Gasda et al.*, 2011; *MacMinn et al.*, 2011]. However, convective dissolution has not been studied experimentally in the context of a gravity current that spreads as it dissolves, and the interaction between these two processes is not understood. In addition, in an aquifer of finite thickness the accumulation of dissolved $CO_2$ in the water beneath the spreading plume may strongly influence the rate of convective dissolution.

[5] Here, we consider the simple model problem of convective dissolution from a buoyant gravity current as it spreads along the top boundary of a vertically confined, horizontal aquifer (Figure 1). We first study this system experimentally using analog fluids. Motivated by our experimental observations, we then study theoretical models for this system based on the well-known theory of gravity currents [*Bear*, 1972; *Huppert and Woods*, 1995], which has recently been used to develop physical insight into $CO_2$ injection [*Lyle et al.*, 2005; *Nordbotten and Celia*, 2006] and postinjection spreading and migration [*Hesse et al.*, 2007, 2008; *Juanes et al.*, 2010; *MacMinn et al.*, 2011; *de Loubens and Ramakrishnan*, 2011; *Golding et al.*, 2011]. We show that the interaction between buoyant spreading, convective dissolution, and the finite thickness of the aquifer has a strong influence on the maximum extent and the lifetime of the buoyant current.

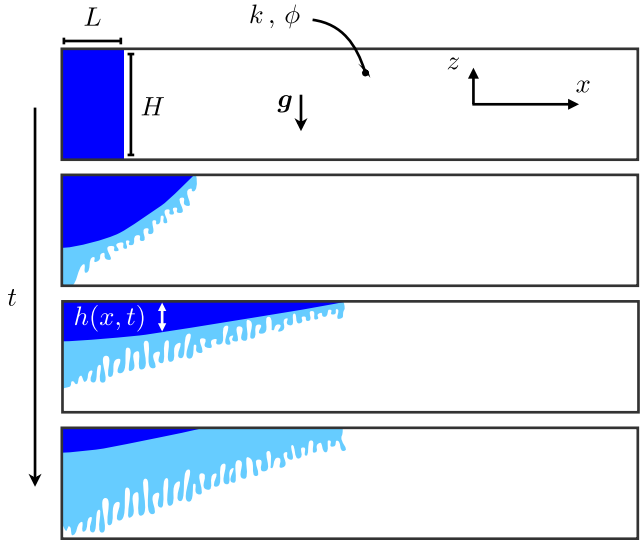


**Figure 1.** A sketch of the simple model problem considered here: a buoyant gravity current (dark blue) spreads beneath a horizontal caprock in a vertically confined aquifer, shrinking as the buoyant fluid dissolves into the ambient fluid via convective dissolution (light blue).

## 2. Experimental System

[6] We consider the instantaneous release of a finite volume of buoyant fluid into a horizontal aquifer. To study this problem experimentally, we work with analog fluids instead of with groundwater and supercritical $CO_2$ because this permits experiments at room temperature and atmospheric pressure, and at laboratory length and time scales.

### 2.1. Analog Fluids

[7] We conduct experiments with water and solutions of methanol and ethylene glycol (MEG) [*Turner and Yang*, 1963; *Turner*, 1966; *Huppert et al.*, 1986]. MEG solutions with ethylene glycol mass fractions less than about 0.68 are less dense than water, so such MEG solutions play the role of the buoyant $CO_2$ while water plays the role of the relatively dense, ambient groundwater [*Neufeld et al.*, 2010]. A buoyant gravity current of MEG spreading over water is subject to convective dissolution because the density of MEG-water mixtures is a nonmonotonic function of MEG mass fraction, and is larger than that of either MEG or water over a range of mass fractions. As a result, the dense mixture of MEG and water that forms along their shared interface drives convective dissolution.

[8] The rate at which a buoyant current of MEG spreads over water is directly proportional to the amount by which the density of the water exceeds the density of the MEG. The rate at which a buoyant current of MEG dissolves into water by convective dissolution scales with the amount by which the maximum density of a MEG-water mixture exceeds the density of water. We denote the former density difference by $\Delta\rho$ and the latter by $\Delta\rho_d^\star$ (Figure 2). A convenient aspect of the MEG-water system is that these two rates can be adjusted relative to one another via the ratio of methanol to ethylene glycol in the pure MEG. Increasing the initial mass fraction of ethylene glycol decreases $\Delta\rho$ but increases $\Delta\rho_d^\star$, leading to slower spreading but faster convective dissolution. Here, we work with two different MEG compositions: 59.1% and 65.4% ethylene glycol by mass, hereafter referred to as "59.1 wt % MEG" and "65.4 wt % MEG," respectively. The latter spreads more slowly but dissolves more quickly than the former. We report the key properties of these two MEG mixtures in Table 1.

[9] Although MEG and water are perfectly miscible, unlike $CO_2$ and water, mixing due to diffusion and dispersion is slow in this system and the initially sharp "interface" between the two fluids is preserved over the duration of the experiment.

### 2.2. Flow Cell

[10] We conduct the experiments in a quasi-two-dimensional flow cell packed with spherical glass beads (Figure 3). The cell is 100 cm long and 15 cm tall, with a 1 cm gap between the plates. The cell is open at the top. We initially divide the cell into two sections via a removable gate, inserted 9 cm from the left edge. After packing both sections with beads following a consistent protocol, we add the buoyant fluid to the smaller, left section and the ambient fluid to the larger, right section. To initiate the experiment, we remove the gate and record the resulting fluid flow with a digital camera. Removal of the gate causes some local bead rearrangement, but this occurs on a much shorter timescale than the flow and has no discernible

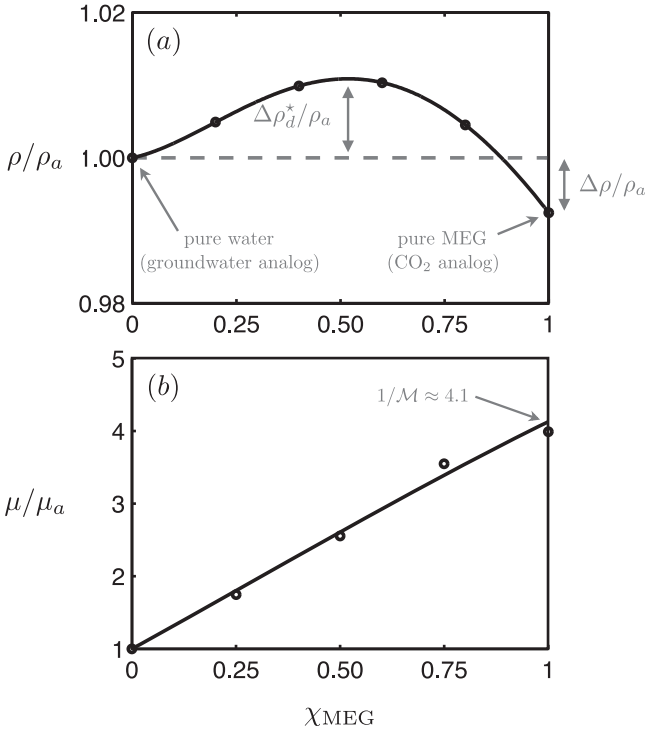


**Figure 2.** (a) The density $\rho$ and (b) viscosity $\mu$ of a MEG-water mixture as a function of MEG mass fraction $\chi_{\mathrm{MEG}}$. Density and viscosity are scaled here by the density $\rho_a$ and viscosity $\mu_a$ of the ambient fluid (water), respectively. Open circles are measurements for a MEG composition of 65.4% ethylene glycol by weight; solid curves are polynomial (Figure 2a) and linear (Figure 2b) best fits to the data. Convective dissolution occurs here because the density of the MEG-water mixture is larger than the density of pure water over a range of MEG mass fractions.

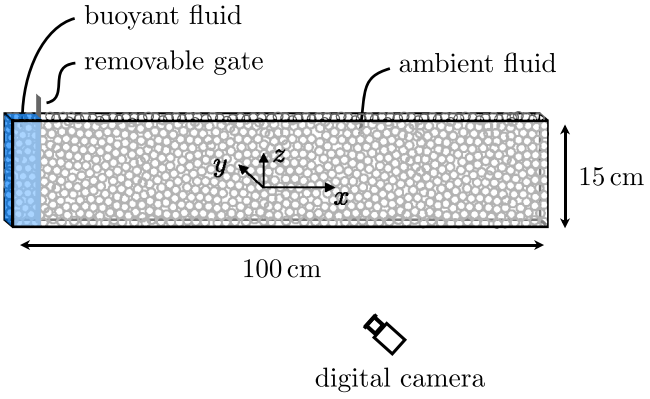


**Figure 3.** Sketch of the quasi-two-dimensional flow cell packed with glass beads in which we conduct the experiments. Before adding the beads and the fluids, we divide the cell into two sections via a removable gate. After filling the cell, we initiate the experiment by removing the gate.

influence on the propagation of the gravity currents or the rate of convective dissolution. After each experiment, we drain the flow cell, remove the beads, and wash and dry both the beads and the cell.

[11] We use the resulting time-lapse images from each experiment to quantify the rate at which the buoyant current spreads by measuring the position $x_N$ of its leading edge or 'nose' as a function of time [e.g., *Huppert*, 1982; *Huppert and Woods*, 1995]. We identify the nose position in the images either by eye or programmatically based on a light intensity threshold; the two methods give similar results because the interface between the two fluids is sharp.

[12] We measure the void fraction or porosity $\phi$ of the bead pack for each experiment directly by measuring the volume of fluid added to the cell during filling. Porosity measurements for different packings of the same bead size were repeatable to within a few percent.

[13] Rather than measuring the permeability of each individual bead pack directly, we instead infer the effective permeability $k$ of these packings from a series of benchmark experiments where a buoyant gravity current of fresh water spreads over ambient saltwater. We review the well-known theoretical model for this problem [*Bear*, 1972; *Huppert and Woods*, 1995] in section 4.1. We prepare and initiate these benchmark experiments following the procedure described at the beginning of this section. Since the rate of spreading is directly proportional to the permeability of the bead pack, and all other parameters are known, we infer the value of the permeability as that which gives the best agreement between the experimental measurements and the predictions of the model (Figure 4). We repeat these measurements several times to ensure reproducibility, and we take the result to be representative of the permeability of all such packings of beads of the same size, prepared following the same protocol.

[14] We work with three different bead sizes, with nominal diameters of 1, 2, and 3 mm. We report the measured porosity and effective permeability of packings of these beads in Table 2. For reference, we also include in Table 2 the permeability $k_{\mathrm{KC}}$ calculated from the Kozeny-Carman relation for a packing with the same porosity of monodisperse spheres with the same nominal diameter. The effective permeability values are in all cases within a factor of about 2 of the values estimated from the Kozeny-Carman relation. The measured values are consistently smaller than the Kozeny-Carman values, which may be due to the fact that the beads were not monodisperse.

**Table 1.** Properties of the Three Pairs of Buoyant and Ambient Fluids Used in the Experiments[a]

| Buoyant Fluid | Ambient Fluid | $\rho_b$ (g cm$^{-3}$) | $\mu_b$ (P) | $\rho_a$ (g cm$^{-3}$) | $\mu_a$ (P) | $\Delta\rho$ (g cm$^{-3}$) | $\Delta\rho_d^\star$ (g cm$^{-3}$) | $\mathcal{M}$ |
|---|---|---|---|---|---|---|---|---|
| 59.1 wt % MEG | water | 0.971 | 0.031 | 0.999 | 0.0095 | 0.028 | 0.0026 | 0.31 |
| 65.4 wt % MEG | water | 0.991 | 0.039 | 0.999 | 0.0095 | 0.008 | 0.0109 | 0.24 |
| Water | saltwater[b] | 0.999 | 0.0095 | 1.007 | 0.0095 | 0.008 | - | 1 |

[a]The symbols used here are defined in the introduction of section 4.
[b]The saltwater is water with 1.075 wt % NaCl.

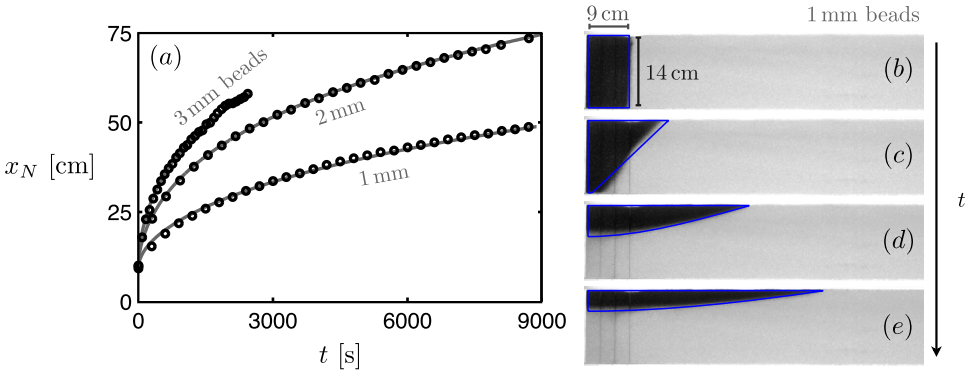


**Figure 4.** (a) The position of the nose of a buoyant current of fresh water spreading over denser salt water with experimental measurements (black circles) and the predictions of the model for a confined gravity current (solid gray curves) for three bead sizes. (b–e) Snapshots of the experiment in 1 mm beads, showing the shape of the current, along with the model predictions (blue curves). We infer the effective permeability of the packed cell from these experiments as that which gives the best fit between the data and the model for each bead size (Table 2). We discuss the model in section 4.1.

## 3. Experimental Results

[15] We first study the spreading and convective dissolution of buoyant currents of the 59.1 wt % MEG. We observe that the nose of the current gradually decelerates until it reaches a maximum position, and subsequently retreats at an accelerating rate until the current dissolves completely. We find that the current typically breaks into a series of discrete patches as it nears complete dissolution (Figure 5).

[16] For buoyant currents of 65.4 wt % MEG, we see different behavior. As with the 59.1 wt % MEG, the nose of the current decelerates, reaches a maximum position, and then retreats to the left. Rather than accelerating on the retreat, however, the nose retreats at a rate that is approximately constant (Figure 6).

[17] The buoyant current of 59.1 wt % MEG advances quickly (driven by $\Delta\rho$) relative to the rate at which water with dissolved MEG falls downward (driven by $\Delta\rho_d^\star$). The buoyant current of 65.4 wt % MEG advances more slowly and dissolves more quickly ($\Delta\rho$ is smaller and $\Delta\rho_d^\star$ is larger), and we observe that water with dissolved MEG reaches the bottom of the flow cell and accumulates there, building and spreading as a dense gravity current. This accumulation increases the density of the ambient fluid beneath the buoyant current, slowing the process of convective dissolution and retarding the retreat of the nose.

## 4. Theoretical Models

[18] We now consider theoretical models for this problem. We assume that the buoyant fluid has constant density $\rho_b$ and viscosity $\mu_b$, and that the ambient fluid has constant density $\rho_a$ and viscosity $\mu_a$. We assume that the aquifer is vertically confined, and has uniform porosity $\phi$, permeability $k$, and thickness $H$ (Figure 1). For simplicity, we consider a planar, two-dimensional system and assume no fluid flow or variations in fluid velocities along the third ($y$) dimension (into the page). The shape of the buoyant current is characterized by its initial length $L$ in the $x$ direction, height $H$ in the $z$ direction, and width $W$ in the $y$ direction, so that the buoyant current initially occupies a volume $\mathcal{V} = LHW$ of the aquifer and contains a corresponding volume $\phi\mathcal{V}$ of buoyant fluid.

**Table 2.** Properties of the Packed Flow Cell for Three Different Nominal Beads Sizes

| Bead Diameter (cm) | $\phi$ | $k$ (cm$^2$) | $k_{KC}$ (cm$^2$) |
|---|---|---|---|
| 0.1 | 0.42 | $8.1 \times 10^{-6}$ | $12 \times 10^{-6}$ |
| 0.2 | 0.44 | $3.5 \times 10^{-5}$ | $5.7 \times 10^{-5}$ |
| 0.3 | 0.45 | $6.0 \times 10^{-5}$ | $15 \times 10^{-5}$ |

[19] We assume vertical flow equilibrium (i.e., the Dupuit approximation), neglecting the vertical component of the fluid velocity relative to the horizontal one and taking the pressure field to be hydrostatic [*Coats et al.*, 1971; *Yortsos*, 1995]. We further neglect the capillary pressure relative to typical gravitational and viscous pressure changes, and also assume that the interface between the two fluids remains sharp. Although both capillary pressure and saturation gradients can be included in such models [*Nordbotten and Dahle*, 2011; *Golding et al.*, 2011], the interaction of these effects with convective dissolution is not clear, and they are not present in our experimental analog system because the fluids are perfectly miscible. Lastly, we require for mass conservation that there be no net flux of fluid through any cross section of the aquifer, because it is vertically confined.

### 4.1. Buoyant Spreading Without Convective Dissolution

[20] In the absence of convective dissolution, the model for the spreading of a buoyant current in a confined porous layer can be written [e.g., *Bear*, 1972, p. 535, equation 9.5.64]

$$\frac{\partial h}{\partial t} - U\frac{\partial}{\partial x}\left[(1-f)h\frac{\partial h}{\partial x}\right] = 0, \tag{1}$$

where $h(x,t)$ is the unknown thickness of the current (Figure 1) and $U = \Delta\rho gk/\phi\mu_b$ is the characteristic buoyancy velocity of the current. The function $f(h)$ is given by

$$f = \frac{\mathcal{M}h}{(\mathcal{M}-1)h + H}, \tag{2}$$

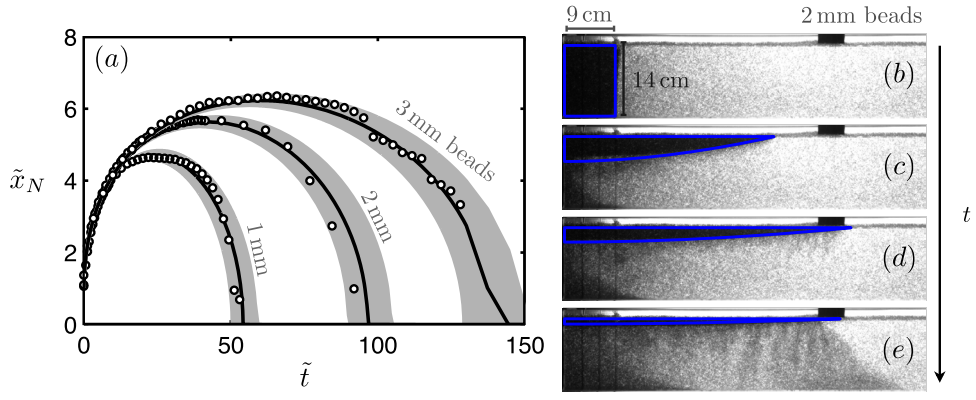


**Figure 5.** (a) The scaled position of the nose of a buoyant current of 59.1 wt % MEG spreading over water with experimental measurements (black circles) and the predictions of the model (solid black curves and gray shaded regions) for three different bead sizes. (b–e) Snapshots of the experiment in 2 mm beads, along with the predictions of the model (blue curves). Nose positions and times in Figure 5a are dimensionless, scaled as discussed in section 4.1. We discuss the model in section 4.2.

with mobility ratio $\mathcal{M} = \mu_a/\mu_b$. The presence of $f(h)$ reflects the fact that the aquifer is vertically confined, so that the buoyant fluid must displace the relatively viscous ambient fluid in order to spread. Flow of the ambient fluid becomes unimportant at late times as the current becomes thin relative to the aquifer thickness ($f(h) \ll 1$ when $h \ll H$). The spreading behavior becomes independent of $\mathcal{M}$ in this unconfined limit [*Barenblatt*, 1996; *Hesse et al.*, 2007].

[21] To rewrite equation (1) in dimensionless form, we define scaled variables

$$\tilde{h} = \frac{h}{H}, \qquad \tilde{t} = \frac{UH}{L^2}t, \qquad \tilde{x} = \frac{x}{L}, \tag{3}$$

and obtain

$$\frac{\partial \tilde{h}}{\partial \tilde{t}} - \frac{\partial}{\partial \tilde{x}}\left[(1-f)\tilde{h}\,\frac{\partial \tilde{h}}{\partial \tilde{x}}\right] = 0. \tag{4}$$

In the unconfined limit, equation (4) has a similarity solution from *Barenblatt* [1952],

$$\tilde{h}(\tilde{x},\tilde{t}) = \frac{1}{6}\tilde{t}^{-1/3}\left(9^{2/3} - \frac{\tilde{x}^2}{\tilde{t}^{2/3}}\right), \tag{5}$$

valid for $|\tilde{x}| \le \tilde{x}_N(\tilde{t})$ and $\tilde{t} > 0$. Equation (5) indicates that the position $\tilde{x}_N$ of the nose of an unconfined current will increase monotonically in time according to the power law

$$\tilde{x}_N(\tilde{t}) = (9\tilde{t})^{1/3}. \tag{6}$$

The solution to equation (4) will converge to equation (5) as the current becomes thin for any initial shape with compact support. The convergence time is small for $\mathcal{M} \ll 1$ and increases strongly with $\mathcal{M}$ [*Hesse et al.*, 2007; *MacMinn and Juanes*, 2009].

[22] We compare the predictions of equation (4) with benchmark experiments in which buoyant water spreads

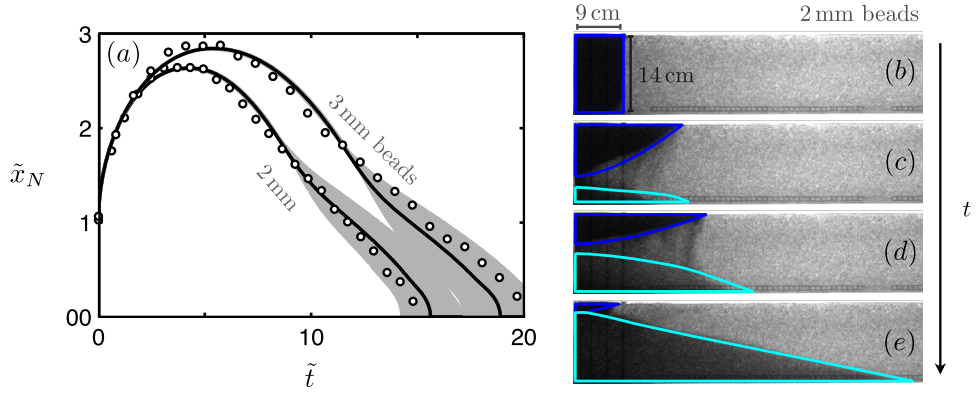


**Figure 6.** (a) The scaled position of the nose of a buoyant current of 65.4 wt % MEG spreading over water with experimental measurements (black circles) and the predictions of the model (solid black curves and gray shaded regions) for two different bead sizes. (b–e) Snapshots of the experiment in 2 mm beads, along with the predictions of the model (blue and cyan curves). Nose position and time are scaled as discussed in section 4.1. We discuss the model in section 4.2.

over ambient saltwater (Figure 4). The ambient saltwater contains 1.075 % NaCl by weight, so the driving density difference is $\Delta\rho = 7.52\,\mathrm{kg\ m^{-3}}$ and the mobility ratio is $\mathcal{M} = 1$ (Table 1). As discussed in section 2.2, we use these experiments to infer the effective permeability of the flow cell.

### 4.2. Buoyant Spreading With Convective Dissolution

[23] Previous studies of convective dissolution have shown that a stationary layer of $CO_2$ will dissolve into a semi-infinite layer of water at a rate that is roughly constant in time [*Hidalgo and Carrera*, 2009; *Kneafsey and Pruess*, 2010; *Pau et al.*, 2010]. When the water layer has a finite thickness, recent results suggest that the dissolution rate is a weak function of the layer thickness [*Neufeld et al.*, 2010; *Backhaus et al.*, 2011], but that it can be approximated as constant provided that the thickness of the $CO_2$ layer is small relative to the thickness of the water layer.

[24] An upscaled model for convective dissolution can then be incorporated into models such as equation (1) by introducing a constant loss or sink term [*Gasda et al.*, 2011; *MacMinn et al.*, 2011],

$$\frac{\partial h}{\partial t} - U\frac{\partial}{\partial x}\left[(1-f)h\,\frac{\partial h}{\partial x}\right] = -\frac{q_d}{\phi}, \tag{7}$$

where the dissolution rate $q_d$ is the volume of buoyant fluid that dissolves per unit bulk fluid-fluid interfacial area per unit time. Rewriting equation (7) in dimensionless form using (3), we obtain

$$\frac{\partial \tilde{h}}{\partial \tilde{t}} - \frac{\partial}{\partial \tilde{x}}\left[(1-f)\tilde{h}\,\frac{\partial \tilde{h}}{\partial \tilde{x}}\right] = -\epsilon, \tag{8}$$

where

$$\epsilon = \left(\frac{L}{H}\right)^2 \frac{q_d}{\phi U} \tag{9}$$

is the dimensionless dissolution rate. *Pritchard et al.* [2001] studied equation (8) in the unconfined limit ($f = 0$) in a different context, developing the explicit solution

$$\tilde{h}(\tilde{x},\tilde{t}) = \frac{1}{6}\tilde{t}^{-1/3}\left(9^{2/3} - \frac{\tilde{x}^2}{\tilde{t}^{2/3}}\right) - \frac{3}{4}\epsilon\tilde{t}, \tag{10}$$

valid for $|\tilde{x}| \le \tilde{x}_N(\tilde{t})$ and $\tilde{t} > 0$. As discussed by *Pritchard et al.* [2001], equation (10) implies that the position of the nose of the current evolves according to

$$\tilde{x}_N(\tilde{t}) = (9\tilde{t})^{1/3}\sqrt{1 - \frac{1}{18}\,\epsilon\,(9\tilde{t})^{4/3}}. \tag{11}$$

Equations (10) and (11) reduce to equations (5) and (6), respectively, when $\epsilon = 0$.

[25] Equation (11) predicts that convective dissolution will have a strong impact on the spreading of the current in the unconfined limit. Without convective dissolution ($\epsilon = 0$), the nose of the current advances for all time following the power law $x_N \propto t^{1/3}$ (equation 6). With convective dissolution, the nose reaches a maximum position $\tilde{x}_N^{\max} = (8/3)^{1/4}\epsilon^{-1/4}$ and then retreats to the origin as the volume of the current decreases to zero at time $\tilde{t}^{\mathrm{end}} = (8/9)^{1/4}\epsilon^{-3/4}$ (Figure 7a). We refer to this time $\tilde{t}^{\mathrm{end}}$ as the 'lifetime' of the current.

[26] The spreading behavior for nonnegligible $\mathcal{M}$ is qualitatively similar to the unconfined behavior predicted by equations (6) and (11), but the current spreads more slowly as $\mathcal{M}$ increases (Figure 7b). Accordingly, the maximum extent of the current decreases with $\mathcal{M}$ while the lifetime of the current increases with $\mathcal{M}$. However, the scalings of these quantities with $\epsilon$ show only minor deviations from the unconfined predictions of $\tilde{x}_N^{\max} \sim \epsilon^{-1/4}$ and $\tilde{t}^{\mathrm{end}} \sim \epsilon^{-3/4}$ (Figure 8).

[27] Equation (10) is not strictly an asymptotic solution of equation (8) because convective dissolution causes some memory of the initial shape to be retained throughout the evolution, as with residual trapping [*Kochina et al.*, 1983; *Barenblatt*, 1996]. In addition, the concept of asymptotics has limited relevance here because the current dissolves completely in finite time.

[28] The predictions of equation (8) are in qualitative agreement with our experimental observations for currents of the faster-spreading, slower-dissolving MEG (59.1 wt %). Quantitative comparison requires an estimate of the dissolution rate $q_d$. Expressions for $q_d$ for a stationary layer have been presented by *Pau et al.* [2010] and *Neufeld et al.* [2010]. The latter, in particular, performed experiments with the same pair of analog fluids used here. Based on those

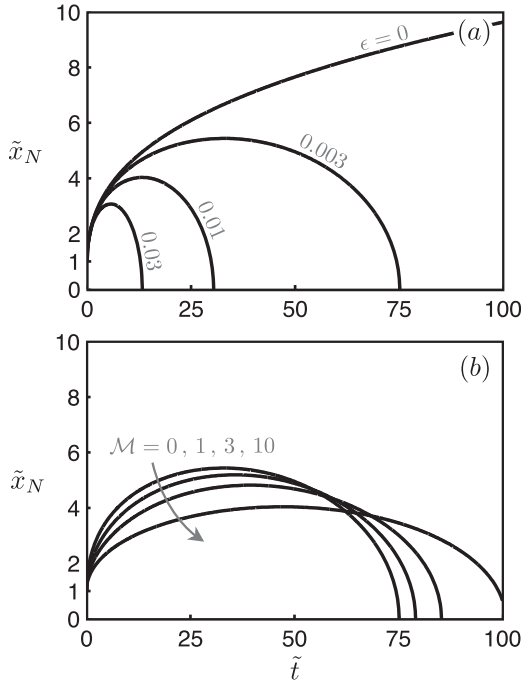


**Figure 7.** (a) Dimensionless nose position against dimensionless time for an unconfined gravity current (i.e., for $\mathcal{M} \ll 1$), as determined from equations (6) and (11) for several values of the dimensionless dissolution rate $\epsilon$. (b) Dimensionless nose position against dimensionless time for a confined gravity current (i.e., for nonnegligible $\mathcal{M}$), as determined from numerical solutions to the confined model (equation (8)) for several values of $\mathcal{M}$ at fixed $\epsilon = 0.003$.

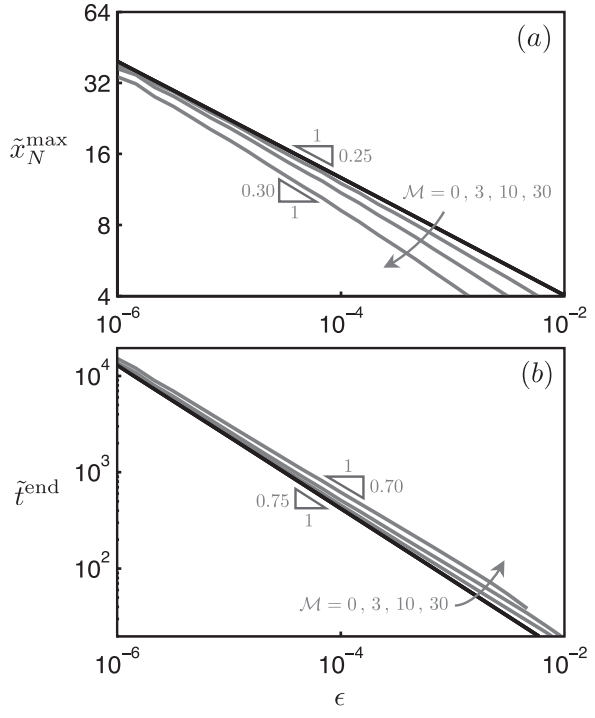


**Figure 8.** (a) The maximum extent $\tilde{x}_N^{\max}$ and (b) the lifetime $\tilde{t}^{\text{end}}$ of a confined gravity current as a function of the dissolution rate $\epsilon$ and for several values of the mobility ratio $\mathcal{M}$. The confined current spreads less far and takes longer to dissolve than the unconfined one, but the ways in which these two quantities scale with $\epsilon$ vary little from the unconfined predictions of $\tilde{x}_N^{\max} \sim \epsilon^{-1/4}$ and $\tilde{t}^{\text{end}} \sim \epsilon^{-3/4}$ (black lines) over the range of $\mathcal{M}$ relevant to $CO_2$ sequestration.

results in conjunction with high-resolution numerical simulations, *Neufeld et al.* [2010] suggested that

$$q_d = b\left(\frac{\phi\chi_v^\star D}{H}\right)\left(\frac{\Delta\rho_d^\star gkH}{\phi\mu_a D}\right)^n, \tag{12}$$

where $\chi_v^\star = \rho_d^\star\chi_m^\star/\rho_b$ measures the volume of buoyant fluid dissolved in one unit volume of ambient fluid containing the maximum (saturated) mass fraction $\chi_m^\star$ of dissolved buoyant fluid, $D \approx 1 \times 10^{-5}\,\text{cm}^2$ is the molecular diffusivity of aqueous buoyant fluid in a porous medium, and $b \approx 0.12$ and $n \approx 0.84$ are dimensionless constants. Although the characteristic vertical scale here should be the depth of the layer of ambient fluid below the buoyant current, we use the total depth of the fluid layer $H \approx 14\,\text{cm}$ for simplicity since the buoyant current is thin for most of its evolution ($h \ll H$). Dissolution due to diffusion and dispersion are not included in this estimate of $q_d$ since these are negligible compared to convective dissolution [*Ennis-King et al.*, 2005].

[29] We begin by estimating the dissolution rate from this expression for 59.1 wt % MEG dissolving into water. We then treat the dissolution rate as a fitting parameter, calibrating its value around this estimate by comparing the predictions of the model with experimental measurements. We present the estimated and calibrated dissolution rates, $q_d^{\text{est}}$ and $q_d$, respectively, in Table 3. The calibrated values are within about a factor of two of the estimated values. That they do not agree exactly is not surprising, given that the correlation of *Neufeld et al.* [2010] was developed in the context of a stationary layer of MEG dissolving into water. Diffusion and flow-induced dispersion in the present context, where the interface has both advancing and receding portions, may enhance or inhibit convective dissolution relative to the case of a stationary layer.

**Table 3.** Parameters for the 59.1 wt % MEG[a]

| Bead Diameter (cm) | $U$ (cm s$^{-1}$) | $q_d^{\text{est}}$ (cm s$^{-1}$) | $q_d$ (cm s$^{-1}$) | $\epsilon$ |
|---|---|---|---|---|
| 0.1 | 0.017 | $0.61 \times 10^{-4}$ | $0.71 \times 10^{-4}$ | $4.6 \times 10^{-3}$ |
| 0.2 | 0.071 | $2.07 \times 10^{-4}$ | $1.21 \times 10^{-4}$ | $2.0 \times 10^{-3}$ |
| 0.3 | 0.120 | $3.29 \times 10^{-4}$ | $1.45 \times 10^{-4}$ | $1.2 \times 10^{-3}$ |

[a]We report the properties of the pure MEG in Table 1. We use $L = 9\,\text{cm}$ and $H \approx 14\,\text{cm}$ in these and all other experiments.

[30] We compare these experiments with the predictions of equation (8) in Figure 5. We compare the evolution of the nose position for all three bead sizes, as well as the evolution of the shape of the current for the 2 mm beads. We include an envelope around the nose position corresponding to $\pm 10\,\%$ around the calibrated dissolution rate $q_d$ to illustrate the sensitivity of the model to this parameter.

[31] These results suggest that the assumption of a constant rate of convective dissolution can capture the qualitative and quantitative features of the impact of convective dissolution on a buoyant current in this system, provided that dissolved buoyant fluid accumulates slowly beneath the buoyant current.

## 5. Two-Current Model for Spreading With Convective Dissolution

[32] Experimental and numerical studies of convective dissolution have thus far focused on dissolution from a stationary layer of $CO_2$ overlying a deep or semi-infinite layer of water. In a confined aquifer, we expect that the accumulation of dissolved $CO_2$ in the water beneath the buoyant current will limit the rate at which the $CO_2$ can dissolve. Here, we extend the model discussed above (equation (8)) to include this accumulation effect in a simple way.

[33] In our experiments with buoyant currents of slower-spreading, faster-dissolving MEG (65.4 wt %), we observed that the accumulation of dissolved MEG in the water played a strong role in the dynamics of the buoyant current. In particular, water with dissolved MEG accumulated on the bottom of the aquifer and slumped downward relative to the ambient fluid because of its larger density. Although the details of convective dissolution and subsequent mass transport are complex, we develop a simple model for this process by assuming that it primarily transports dissolved buoyant fluid vertically from the buoyant current down to a dense current of ambient fluid with dissolved buoyant fluid (Figure 9). We assume that this dense current consists of ambient fluid with a constant and uniform mass fraction $\chi_m$ of dissolved buoyant fluid, with corresponding density $\rho_d$ and viscosity $\mu_d$, and we denote its unknown local thickness by $h_d(x,t)$. Note that $\chi_m$ may be less than the maximum (saturated) mass fraction $\chi_m^\star$. We

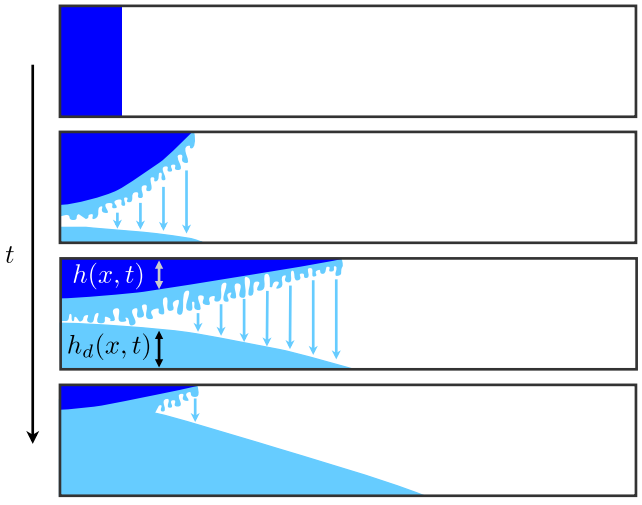


**Figure 9.** A sketch of the two-current model where dissolved buoyant fluid accumulates in a dense gravity current (light blue) that grows and spreads along the bottom of the aquifer as the buoyant current (dark blue) shrinks and spreads along the top.

assume that convective dissolution transfers fluid from the buoyant current to the dense current at a constant rate except where the ambient fluid is locally saturated, which we assume occurs where the buoyant current and the dense current touch ($h + h_d = 1$). For simplicity, we assume that buoyant fluid accumulates in the dense current at the same position $x$ and time $t$ at which it dissolved from the buoyant current.

[34] Applying Darcy's law and conservation of mass for this system, and assuming sharp interfaces and vertical flow equilibrium as discussed at the beginning of section 4 above, we have in dimensionless form

$$\frac{\partial \tilde{h}}{\partial \tilde{t}} - \frac{\partial}{\partial \tilde{x}}\left[(1-f)\tilde{h}\,\frac{\partial \tilde{h}}{\partial \tilde{x}} - \delta f \tilde{h}_d\,\frac{\partial \tilde{h}_d}{\partial \tilde{x}}\right] = -\tilde{\epsilon} \tag{13}$$

$$\frac{\partial \tilde{h}_d}{\partial \tilde{t}} - \frac{\partial}{\partial \tilde{x}}\left[\delta(1-f_d)\tilde{h}_d\,\frac{\partial \tilde{h}_d}{\partial \tilde{x}} - f_d \tilde{h}\,\frac{\partial \tilde{h}}{\partial \tilde{x}}\right] = \frac{\tilde{\epsilon}}{\chi_v}, \tag{14}$$

where $\tilde{h}$, $\tilde{x}$, and $\tilde{t}$ are as defined in equation (3). The nonlinear function $f$ now includes the presence of the dense current,

$$f = \frac{\mathcal{M}h}{(\mathcal{M}-1)h + (\mathcal{M}_d - 1)h_d + 1} \tag{15}$$

and we have a second such function

$$f_d = \frac{\mathcal{M}_d h_d}{(\mathcal{M}-1)h + (\mathcal{M}_d - 1)h_d + 1}. \tag{16}$$

Finally, we redefine the dimensionless convective dissolution rate $\epsilon$ to be conditional,

$$\epsilon = \begin{cases} (L/H)^2\,(q_d/\phi U) & \text{if } h + h_d < 1, \\ 0 & \text{if } h + h_d = 1, \end{cases} \tag{17}$$

so that it takes a constant, nonzero value where the buoyant current and the dense one are separate and vanishes where they are touching.

[35] This two-current model contains three new parameters relative to the simpler model: $\mathcal{M}_d = \mu_a/\mu_d$, which is the ratio of the viscosity of the ambient fluid, $\mu_a$, to that of the dense mixture, $\mu_d$; $\delta = U_d/U = (\Delta\rho_d/\mu_d)/(\Delta\rho/\mu_b)$, which is the ratio of the characteristic buoyancy velocity of the dense current, $U_d = (\rho_d - \rho_a)gk/\phi\mu_d$, to that of the buoyant one, $U$; and $\chi_v = \rho_d\chi_m/\rho_b \le \chi_v^\star$, which is the volume fraction of buoyant fluid dissolved in the dense current at mass fraction $\chi_m$. All three of these parameters are uniquely defined by the properties of the buoyant and ambient fluids, the value of $\chi_m$, and appropriate constitutive relations $\rho_d(\chi)$ and $\mu_d(\chi)$ for the mixture.

[36] The buoyant current loses volume due to convective dissolution at a rate $\epsilon$ per unit length, and this volume is transferred to the dense current at a rate $\epsilon/\chi_v$ per unit length. This model reduces to the simpler model (equation (8)) for $\chi_v \to \infty$, when one unit volume of the dense current can hold an arbitrary amount of dissolved buoyant fluid so that the dense current does not accumulate no matter how much buoyant fluid dissolves.

[37] We solve equations (13) and (14) numerically. To do so, we discretize the two equations in space using a second-order finite-volume method to guarantee conservation of volume. We then integrate the two equations in time using a first-order explicit method, which greatly simplifies the handling of the coupling between these two nonlinear conservation laws. Explicit time integration requires small, local corrections to the mass transfer between the two currents at the end of each time step in order to avoid local overshoot where the dense current rises to meet the buoyant one.

[38] We find that the accumulation of the dense current strongly inhibits convective dissolution from the buoyant current, leading to a marked departure from the behavior predicted by the single-current model when the two currents touch (Figure 10).

[39] The predictions of this model are in qualitative agreement with our experimental observations for the slower-spreading, faster-dissolving MEG (65.4 wt %). Quantitative comparison requires an estimate of the dissolution rate $q_d$ and the mass fraction $\chi_m$ of dissolved MEG in the lower layer. As discussed above, the parameters $\chi_v$, $M_d$, and $\delta$ are then calculated from $\chi_m$ based on the constitutive relations for MEG-water mixtures (Figure 2).

[40] We again estimate $q_d$ from equation (12), and then calibrate $q_d$ around this estimated value in order to match the early time spreading behavior, during which time the dense current plays little role. We develop an initial estimate of the mass fraction $\chi_m$ of MEG in the dense current based on the final volume of the dense current once the buoyant current has completely dissolved, and we then calibrate $\chi_m$ around this value. We report these values in Table 4.

[41] We compare the predictions of this model with our experiments with the slower-spreading, faster-dissolving MEG (65.4 wt %) in Figure 6. We compare the evolution of the nose position for two bead sizes, as well as the evolution of the shape of the buoyant current for the 2 mm beads. We include an envelope around the nose position corresponding to $\pm 5$ % around the calibrated mass fraction $\chi_m$. The nose position is quite sensitive to this quantity since

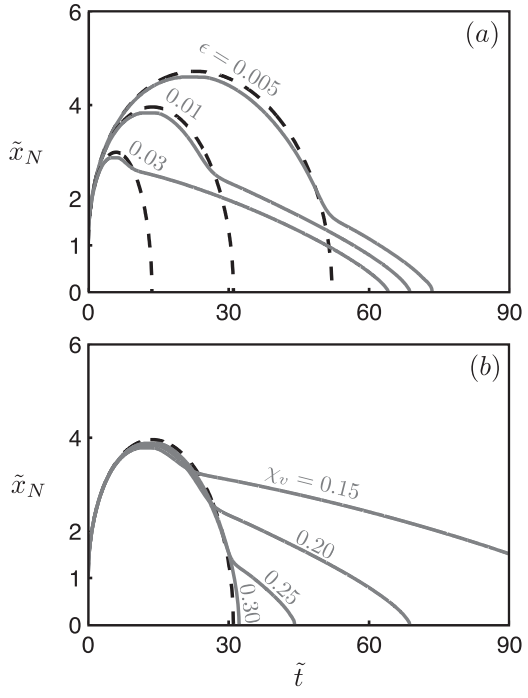


**Figure 10.** (a) The evolution of the nose of the buoyant current from numerical solutions to the two-current model for several values of $\epsilon$ without (dashed black lines) and with (solid gray lines) accumulation. The presence of the dense current retards the nose of the buoyant current weakly due to hydrodynamic interactions before the two currents touch and then strongly by inhibiting convective dissolution after the two currents touch ($\mathcal{M} = 0.25$, $\mathcal{M}_d = 1$, $\delta = 1.1$, $\chi_v = 0.2$). (b) Solutions for $\epsilon = 0.01$ and several values of $\chi_v$ (other parameters unchanged). The two currents touch earlier as $\chi_v$ decreases, and the nose retreats more slowly thereafter.

varying it here changes the time at which the two currents touch and the subsequent rate of retreat (Figure 10b), and also the properties of the dense current via the parameters $\delta$ and $\mathcal{M}_d$.

[42] These results suggest that this model captures the fundamental impact of the accumulation of dissolved buoyant fluid in the ambient water. However, one limitation of this model is that we do not have an a priori estimate of the mass fraction $\chi_m$, and the model is very sensitive to this quantity. To develop such an estimate will require further experiments and high-resolution numerical simulations to study the accumulation of dissolved buoyant fluid. Also, although we have assumed that convective dissolution ceases locally when the two currents touch, the fact that $\chi_m$ is less than the maximum value $\chi_m^\star$ implies that convective dissolution may continue at a reduced rate after the two currents touch since it remains possible to generate mixtures at the interface that are denser than the surrounding fluid. The comparison between this model and our experimental results implies that this model captures the fundamental behavior of the MEG-water system, but further study will be necessary to assess the limits of this model in practice.

## 6. Application to Carbon Sequestration

[43] We now consider these results in the context of $CO_2$ sequestration in a saline aquifer. A key difference between the MEG-water system and the $CO_2$-water system is that MEG and water are fully miscible, whereas $CO_2$ and water are immiscible. Although the impact of capillarity on convective dissolution is unknown, it has been shown that the impact of capillarity on the spreading of a gravity current is negligible when the capillary pressure is small relative to typical gravitational and viscous pressure changes [*Nordbotten and Dahle*, 2011; *Golding et al.*, 2011]. We assume that this is also the case for convective dissolution. We next compare the dimensionless parameters for the $CO_2$-water system with those for the MEG-water system.

[44] Motivated by the Sleipner site in the North Sea, we consider an aquifer for which $\rho_b \approx 500\,\mathrm{kg\,m^{-3}}$, $\mu_b \approx 4 \times 10^{-5}$ Pa s, $\rho_a \approx 1000\,\mathrm{kg\,m^{-3}}$, and $\mu_a \approx 6 \times 10^{-4}$ Pa s [*Bickle et al.*, 2007], giving a mobility ratio of $\mathcal{M} \approx 15$. This value of $\mathcal{M}$ is much larger than in the MEG-water system ($\mathcal{M} \approx 0.31$ for the 59.11 wt % MEG and $\approx 0.24$ for the 65.4 wt % MEG). As a result, the $CO_2$ plume will be much more strongly tongued than the MEG plume, presenting much more interfacial area for convective dissolution and increasing its effectiveness [*MacMinn et al.*, 2011].

[45] For an aquifer of thickness $H \approx 20\,\mathrm{m}$, porosity $\phi \approx 0.375$, and permeability $k \approx 2.5 \times 10^{-12}\,\mathrm{m^2}$, the characteristic spreading rate of the $CO_2$ plume is $U \approx 5.8 \times 10^{-5}\,\mathrm{m\,s^{-1}}$ and *Neufeld et al.* [2010] estimated the dissolution rate to be $q_d \approx 1 \times 10^{-9}\,\mathrm{m\,s^{-1}}$. The estimate of *Pau et al.* [2010] for the dissolution rate in the Carrizo-Wilcox aquifer in Texas is of the same order. For a relatively large sequestration project in such an aquifer, where $M \approx 10\,\mathrm{Mt}$ of $CO_2$ is injected along a linear array of wells [*Nicot*, 2008] of length $W \approx 10\,\mathrm{km}$, the characteristic length is $L = M/2\rho_b\phi HW \approx 130$ m and the corresponding dimensionless dissolution rate is $\epsilon = q_d L^2/\phi U H^2 \approx 0.002$. Although quite sensitive to the specific injection scenario, this value is comparable to the values from our experiments

**Table 4.** Parameters for the 65.4 wt % MEG[a]

| Bead Diameter (cm) | $U$ (cm s$^{-1}$) | $q_d^{\mathrm{est}}$ (cm s$^{-1}$) | $q_d$ (cm s$^{-1}$) | $\epsilon$ | $\chi_v$ | $\mathcal{M}_d$ | $\delta$ |
|---|---|---|---|---|---|---|---|
| 0.1 | $3.6 \times 10^{-3}$ | $2.0 \times 10^{-4}$ | $1.8 \times 10^{-4}$ | 0.055 | 0.30 | 0.51 | 2.14 |
| 0.2 | $1.5 \times 10^{-2}$ | $6.8 \times 10^{-4}$ | $6.8 \times 10^{-4}$ | 0.040 | 0.30 | 0.51 | 2.14 |
| 0.3 | $2.5 \times 10^{-2}$ | $1.1 \times 10^{-3}$ | $8.2 \times 10^{-4}$ | 0.028 | 0.28 | 0.53 | 2.06 |

[a]We report the properties of the pure MEG in Table 1. We use $L = 9\,\mathrm{cm}$ and $H \approx 14\,\mathrm{cm}$ in these and all other experiments. Here $\chi_m$ and $\chi_v$ are approximately equal.

($\epsilon \approx 0.001$–$0.005$ for the 59.11 wt % MEG and $\approx 0.03$–$0.06$ for the 65.4 wt % MEG).

[46] Unlike in our experiments, the solubility of $CO_2$ in groundwater is only a few percent by weight at typical aquifer conditions [*Duan and Sun*, 2003]. For $\chi_m \approx 0.01$, the corresponding increase in the density of the water is $\Delta\rho_d \approx 10\,\mathrm{kg\,m^{-3}}$ [*García*, 2001] and the change in its viscosity is negligible, so we expect $\chi_v \approx 0.02$, $\delta \approx 0.02$, and $\mathcal{M}_d \approx 1$. These values of $\chi_v$ and $\delta$ are about an order of magnitude smaller than those in our experiments.

[47] Based on these values of $\epsilon$, $\delta$, and $\chi_v$, we expect dissolved $CO_2$ to accumulate very quickly and slump downward very slowly relative to the rate at which the buoyant current spreads. As a result, we expect the rate at which $CO_2$ is trapped to be controlled not by the rate of convective dissolution, but by the amount of dissolved $CO_2$ the water can hold (i.e., $\chi_v$) and by the rate at which this water slumps downward. In Figure 11, we show that this is indeed the case: both the maximum extent and the lifetime of a plume of $CO_2$ decrease as the dissolution rate increases, but both quantities approach limiting values that are independent of the dissolution rate if this rate is sufficiently large. The dissolution rate of $\epsilon \approx 0.002$ estimated above is about 2 orders of magnitude above this threshold value. As a result, the spreading and convective dissolution of the plume is completely controlled by the accumulation of dissolved $CO_2$ in this setting, and the plume spreads several times further and persists for several orders of magnitude longer than it would without this accumulation.

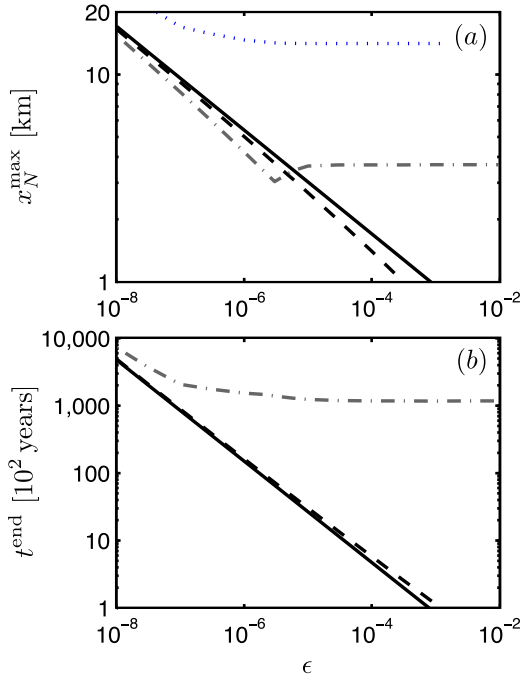


**Figure 11.** (a) The maximum extent $x_N^{\max}$ and (b) the lifetime $t^{\mathrm{end}}$ of a buoyant plume of $CO_2$ spreading in a saline aquifer as a function of the dissolution rate $\epsilon$ in the unconfined limit (solid black curve), from a numerical solution of equation (8) (dashed black curve), and from a numerical solution of the two-layer model (dash-dotted gray curve). We also show in Figure 11a the position of the nose of the dense current at time $t^{\mathrm{end}}$ (dotted blue curve). Parameters are appropriate for the Sleipner formation, as discussed in section 6.

## 7. Discussion and Conclusions

[48] We have shown via experiments with analog fluids that simple models are able to capture the impact of convective dissolution on the spreading of a buoyant gravity current in a vertically confined, horizontal layer.

[49] When dissolved buoyant fluid accumulates slowly beneath the buoyant current, our experiments have confirmed that the complex dynamics of convective dissolution can be upscaled to a constant mass flux [*Pau et al.*, 2010; *Kneafsey and Pruess*, 2010; *Neufeld et al.*, 2010] and incorporated into a simple model [*Gasda et al.*, 2011; *MacMinn et al.*, 2011] (Figure 5).

[50] When dissolved buoyant fluid accumulates quickly beneath the buoyant current, our experiments have shown that this accumulation can have an important limiting effect on the dissolution process. To capture the accumulation of dissolved buoyant fluid, we have developed a two-current model where a dense gravity current of ambient fluid with dissolved buoyant fluid grows and spreads along the bottom of the aquifer. We have used this model to show that the accumulation of dissolved buoyant fluid beneath the buoyant current can slow convective dissolution, and we have confirmed this prediction experimentally (Figure 6).

[51] Using this two-current model, we have shown that we expect $CO_2$ spreading and dissolution in a horizontal aquifer to be controlled primarily by the mass fraction at which $CO_2$ accumulates in the water, and to be nearly independent of the dissolution rate (Figure 11). This can be the case even in the presence of aquifer slope or background groundwater flow, both of which drive net $CO_2$ migration and expose the plume to fresh water, when slope- or flow-driven migration is sufficiently slow [*MacMinn et al.*, 2011].

[52] The planar models used here rely on the fact that the transverse width of the buoyant current is much larger than its length in the $x$ direction, $W \gg L$, which is typically the case when large amounts of $CO_2$ are injected via a line drive configuration [*Nicot*, 2008; *Szulczewski et al.*, 2012]. The models presented here can be readily adapted to a radial geometry for injection from a single well where appropriate. Where neither geometric approximation is appropriate, use of a more complicated, two-dimensional model will be necessary.

[53] We have also assumed here an idealized rectangular initial shape for the plume of $CO_2$. In practice, the specific details of the injection scenario will have some quantitative impact on the maximum extent and lifetime of the $CO_2$, but should have little qualitative impact on the interaction between plume spreading, convective dissolution, and the accumulation of dissolved $CO_2$.

[54] **Acknowledgments.** C.W.M. gratefully acknowledges the support of a David Crighton Fellowship and a Yale Climate and Energy Institute Postdoctoral Fellowship. J.A.N. is supported by a Royal Society University Research Fellowship. The work of H.E.H. is partially supported by a Royal Society Wolfson Research Merit Award. M.A.H. acknowledges support by the U.S. Department of Energy's National Energy Technology Laboratory under DE-FE0001563. The views expressed herein do not necessarily reflect those of the U.S. government or any agency thereof.

## References


Backhaus, S., K. Turitsyn, and R. E. Ecke (2011), Convective instability and mass transport of diffusion layers in a Hele-Shaw geometry, *Phys. Rev. Lett.*, *106*(10), 104501.

Barenblatt, G. I. (1952), On some unsteady motions of fluids and gases in a porous medium [in Russian], *Appl. Math. Mech.*, *16*(1), 67–78.

Barenblatt, G. I. (1996), *Scaling, Self-Similarity, and Intermediate Asymptotics*, Cambridge Univ. Press, Cambridge, U. K.

Bear, J. (1972), *Dynamics of Fluids in Porous Media*, Elsevier, New York.

Bickle, M. J. (2009), Geological carbon storage, *Nat. Geosci.*, *2*, 815–818.

Bickle, M., A. Chadwick, H. E. Huppert, M. Hallworth, and S. Lyle (2007), Modeling carbon dioxide accumulation at Sleipner: Implications for underground carbon storage, *Earth Planet. Sci. Lett.*, *255*(1–2), 164–176.

Coats, K. H., J. R. Dempsey, and J. H. Henderson (1971), The use of vertical equilibrium in two-dimensional simulations of three-dimensional reservoir performance, *SPE J.*, *11*(1), 63–71.

de Loubens, R., and T. S. Ramakrishnan (2011), Analysis and computation of gravity-induced migration in porous media, *J. Fluid. Mech.*, *675*, 60–86.

Duan, Z., and R. Sun (2003), An improved model calculating $CO_2$ solubility in pure water and aqueous NaCl solutions from 273 to 533 K and from 0 to 2000 bar, *Chem. Geol.*, *193*(3–4), 257–271.

Ennis-King, J., I. Preston, and L. Paterson (2005), Onset of convection in anisotropic porous media subject to a rapid change in boundary conditions, *Phys. Fluids*, *17*, 084107.

García, J. (2001), Density of aqueous solutions of $CO_2$, report, Lawrence Berkeley Natl. Lab., Berkeley, Calif. [Available at http://www.escholarship.org/uc/item/6dn022hb.]

Gasda, S. E., J. M. Nordbotten, and M. A. Celia (2011), Vertically averaged approaches for $CO_2$ migration with solubility trapping, *Water Resour. Res.*, *47*, W05528, doi:10.1029/2010WR009075.

Golding, M. J., J. A. Neufeld, M. A. Hesse, and H. E. Huppert (2011), Two-phase gravity currents in porous media, *J. Fluid. Mech.*, *678*, 248–270.

Hesse, M. A., H. A. Tchelepi, B. J. Cantwell, and F. M. Orr Jr. (2007), Gravity currents in horizontal porous layers: Transition from early to late self-similarity, *J. Fluid. Mech.*, *577*, 363–383.

Hesse, M. A., F. M. Orr Jr., and H. A. Tchelepi (2008), Gravity currents with residual trapping, *J. Fluid. Mech.*, *611*, 35–60.

Hidalgo, J., and J. Carrera (2009), Effect of dispersion on the onset of convection during $CO_2$ sequestration, *J. Fluid. Mech.*, *640*, 441–452.

Huppert, H. E. (1982), The propagation of two-dimensional and axisymmetric viscous gravity currents over a rigid horizontal surface, *J. Fluid. Mech.*, *121*, 43–58.

Huppert, H. E., and A. W. Woods (1995), Gravity-driven flows in porous layers, *J. Fluid. Mech.*, *292*, 55–69.

Huppert, H. E., J. S. Turner, S. N. Carey, R. Stephen, J. Sparks, and M. A. Hallworth (1986), A laboratory simulation of pyroclastic flows down slopes, *J. Volcanol. Geotherm. Res.*, *30*(3–4), 179–199.

Intergovernmental Panel on Climate Change (2005), *Carbon Dioxide Capture and Storage, Special Report Prepared by Working Group III of the Intergovernmental Panel on Climate Change*, Cambridge Univ. Press, Cambridge, U. K.

Juanes, R., C. W. MacMinn, and M. L. Szulczewski (2010), The footprint of the $CO_2$ plume during carbon dioxide storage in saline aquifers: Storage efficiency for capillary trapping at the basin scale, *Transp. Porous Media*, *82*(1), 19–30.

Kneafsey, T. J., and K. Pruess (2010), Laboratory flow experiments for visualizing carbon dioxide-induced, density-driven brine convection, *Transp. Porous Media*, *82*(1), 123–139.

Kochina, I. N., N. N. Mikhailov, and M. V. Filinov (1983), Groundwater mound damping, *Int. J. Eng. Sci.*, *21*(4), 413–421.

Lackner, K. S. (2003), Climate change: A guide to $CO_2$ sequestration, *Science*, *300*(5626), 1677–1678.

Lindeberg, E., and D. Wessel-Berg (1997), Vertical convection in an aquifer column under a gas cap of $CO_2$, *Energy Convers. Manage.*, *38*, S229–S234.

Lyle, S., H. E. Huppert, M. Hallworth, M. Bickle, and A. Chadwick (2005), Axisymmetric gravity currents in a porous medium, *J. Fluid. Mech.*, *543*, 293–302.

MacMinn, C. W., and R. Juanes (2009), Post-injection spreading and trapping of $CO_2$ in saline aquifers: Impact of the plume shape at the end of injection, *Comput. Geosci.*, *13*(4), 483–491.

MacMinn, C. W., M. L. Szulczewski, and R. Juanes (2011), $CO_2$ migration in saline aquifers. Part 2. Capillary and solubility trapping, *J. Fluid. Mech.*, *688*, 321–351.

Neufeld, J. A., M. A. Hesse, A. Riaz, M. A. Hallworth, H. A. Tchelepi, and H. E. Huppert (2010), Convective dissolution of carbon dioxide in saline aquifers, *Geophys. Res. Lett.*, *37*, L22404, doi:10.1029/2010GL044728.

Nicot, J.-P. (2008), Evaluation of large-scale $CO_2$ storage on fresh-water sections of aquifers: An example from the Texas Gulf Coast Basin, *Int. J. Greenhouse Gas Control*, *2*(4), 582–593.

Nordbotten, J. M., and M. A. Celia (2006), Similarity solutions for fluid injection into confined aquifers, *J. Fluid. Mech.*, *561*, 307–327.

Nordbotten, J. M., and H. K. Dahle (2011), Impact of the capillary fringe in vertically integrated models for $CO_2$ storage, *Water Resour. Res.*, *47*, W02537, doi:10.1029/2009WR008958.

Orr, F. M., Jr. (2009), Onshore geologic storage of $CO_2$, *Science*, *325*(5948), 1656–1658.

Pau, G. S. H., J. B. Bell, K. Pruess, A. S. Almgren, M. J. Lijewski, and K. Zhang (2010), High-resolution simulation and characterization of density-driven flow in $CO_2$ storage in saline aquifers, *Adv. Water Resour.*, *33*(4), 443–455.

Pritchard, D., A. W. Woods, and A. J. Hogg (2001), On the slow draining of a gravity current moving through a layered permeable medium, *J. Fluid. Mech.*, *444*, 23–47.

Riaz, A., M. Hesse, H. A. Tchelepi, and F. M. Orr Jr. (2006), Onset of convection in a gravitationally unstable diffusive boundary layer in porous media, *J. Fluid. Mech.*, *548*, 87–111.

Slim, A. C., and T. S. Ramakrishnan (2010), Onset and cessation of time-dependent, dissolution-driven convection in porous media, *Phys. Fluids*, *22*(12), 124103.

Szulczewski, M. L., C. W. MacMinn, H. J. Herzog, and R. Juanes (2012), Lifetime of carbon capture and storage as a climate-change mitigation technology, *Proc. Natl. Acad. Sci. U. S. A.*, *109*(14), 5185–5189.

Turner, J. S. (1966), Jets and plumes with negative or reversing buoyancy, *J. Fluid. Mech.*, *26*, 779–792.

Turner, J. S., and I. K. Yang (1963), Turbulent mixing at the top of stratocumulus clouds, *J. Fluid. Mech.*, *17*, 212–224.

Weir, G. J., S. P. White, and W. M. Kissling (1996), Reservoir storage and containment of greenhouse gases, *Transp. Porous Media*, *23*(1), 37–60.

Yortsos, Y. C. (1995), A theoretical analysis of vertical flow equilibrium, *Transp. Porous Media*, *18*(2), 107–129.